Nano Research 2017, 10(9): 3103–3112
DOI 10.1007/s12274-017-1527-1
Research Article
ISSN 1998-0124
CN 11-5974/O4

Au/$Ni_{12}P_5$ core/shell single-crystal nanoparticles as oxygen evolution reaction catalyst

Yingying Xu[1,§], Sibin Duan[1,§], Haoyi Li[2], Ming Yang[3], Shijie Wang[3], Xun Wang[2], and Rongming Wang[1] (✉)

[1] *Beijing Key Laboratory for Magneto-Photoelectrical Composite and Interface Science, School of Mathematics and Physics, University of Science and Technology Beijing, Beijing 100083, China*
[2] *Department of Chemistry, Tsinghua University, Beijing 100084, China*
[3] *Institute of Materials Research and Engineering, A*STAR, 2 Fusionopolis Way, Singapore 138634, Singapore*
[§] *Yingying Xu and Sibin Duan contributed equally to this work.*

Received: 25 November 2016
Revised: 10 February 2017
Accepted: 11 February 2017

KEYWORDS
oxygen evolution reaction, nickel phosphide, core/shell nanoparticles, interfacial coupling

ABSTRACT

We have demonstrated the improved performance of oxygen evolution reactions (OER) using Au/nickel phosphide ($Ni_{12}P_5$) core/shell nanoparticles (NPs) under basic conditions. NPs with a $Ni_{12}P_5$ shell and a Au core, both of which have well-defined crystal structures, have been prepared using solution-based synthetic routes. Compared with pure $Ni_{12}P_5$ NPs and Au-$Ni_{12}P_5$ oligomer-like NPs, the core/shell crystalline structure with Au shows an improved OER activity. It affords a current density of 10 mA/cm^2 at a small overpotential of 0.34 V, in 1 M KOH aqueous solution at room temperature. This enhanced OER activity may relate to the strong structural and effective electronic coupling between the single-crystal core and the shell.

1 Introduction

In the pursuit of sustainable energy, the hydrogen cycle has attracted considerable attention as hydrogen is a clean, non-polluting, and CO_2-free energy carrier for energy storage options. However, hydrogen production processes such as direct solar [1] and electricity-driven [2] water splitting ($H_2O \rightarrow H_2 + O_2$) are always associated with substantial energy losses. Most of the overpotential giving rise to the energy loss is related to the oxygen evolution process. The design of cost-effective, highly active catalytic electrodes for oxygen evolution reactions (OERs) has become a critical topic in water splitting. In order to develop highly active catalysts based on abundant elements, some oxides of first-row transition metals (Co, Mn, Ni, Fe, etc.) have been extensively studied as electrode materials [3–6], in contrast to the well-known noble metal oxide catalysts (such as RuO_2 and IrO_2 [7, 8]). These ceramic oxides with the spinel (such as Co_3O_4 [3, 4] and $NiCo_2O_4$ [5]) or perovskite (mainly $LaNiO_3$, $LaCoO_3$ [6], etc.) structures exhibit efficient electrochemical activity

Address correspondence to rmwang@ustb.edu.cn

for OER, as well as high electronic conductivity and stability in alkaline solutions.

Other non-metal elements like B, N, P, or S have also been explored to improve the activities of metal electrocatalysts in recent works [2, 9–13]. In order to further lower the overpotential in water splitting, other kinds of transition metal compounds with considerable conductivity and stability have been successfully used as catalysts in OER, including metal sulfides (Ni_3S_2) [9], nitrides (CoN) [10], and phosphates (Co-Pi) [2, 13]. Transition metal phosphides (Ni_2P, Co_2P, Fe_2P, etc.) are well known as a group of stable catalysts with promising high-activity in fuel hydroprocessing technology [14, 15] and organic dye degradation [16, 17]. Recently, they have also been shown to have promising electrochemical catalytic performance in water splitting, especially in hydrogen evolution reactions (HER) [18–22]. In addition, the physical properties of the metal phosphides are desirable for application as electrochemical catalytic electrodes. It is reported that metal-rich phosphides are good conductors of heat and electricity (resistivity < 200 μΩ·cm) similar to metals, with hardness and strength close to those of ceramics. These phosphides also display high thermal and chemical stability [15].

One way to achieve a large reaction surface and tunable activity in catalytic design is to develop nanostructured catalysts. By adjusting the components and their interface, heterostructured catalysts can provide the desired flexibility. Due to their synergetic effects, the coupling interaction between the catalyst and the substrate can lead to high OER activity. It is reported that the OER turnover frequency (TOF) for ~0.4 monolayer (ML) of cobalt oxide deposited on Au is nearly three times higher than that for bulk Ir [23], due to the strain or structural deformation in the nanostructure, which modifies the reactivity of the nanostructure surface and the energy levels of the bonding electrons [24]. The catalytic activity and selectivity can be further improved by tuning the stress in the nanostructures.

Compared with other systems such as thin films, the core/shell nanoparticle (NP) structure is one of the most effective ways to induce stress. Stress in the core/shell NPs may come from the finite size effect, defects, surface reconstruction, interfacial lattice mismatch, or interfacial interactions between the core and the shell [24]. With substantial lattice constant mismatches at the core/shell interfaces, homogenous strain distribution and strong coupling effects can be induced in single-crystal hybrid metal/semiconductor core/shell heterostructures [25, 26]. It is believed that these strong coupling interactions could induce core/shell synergetic effects and enhance the catalytic performance.

In this study, we report that NPs consisting of a single crystalline nickel phosphide ($Ni_{12}P_5$) shell and a Au core display efficient OER catalytic ability. The synthesized Au/$Ni_{12}P_5$ core/shell NPs can afford a current density of 10 mA/cm^2 at a small overpotential of 0.34 V in 1 M KOH aqueous solution, which is much improved compared with that of Au-$Ni_{12}P_5$ oligomer-like and pure $Ni_{12}P_5$ NPs.

2 Experimental

The Au/$Ni_{12}P_5$ core/shell NPs are synthesized via a solution-based route [27], using the *in situ* transition method based on our previous work [26]. In a typical synthesis, $Ni(acac)_2$ (0.5 g) is dissolved in 10 mL oleylamine (OAm), and then heated up to 100 ℃ for 60 min, forming a blue-green solution. After that, a freshly prepared solution of $HAuCl_4{\cdot}4H_2O$ (0.05 g in 5 mL of toluene) was added dropwise with stirring and maintained at 100 ℃ for 120 min. Then, triphenylphosphine (TPP) (1.0 g) was added and the reaction stirred for 60 min. The solution was then heated to 270 ℃ for 180 min and then cooled to room temperature. Finally, the prepared Au/$Ni_{12}P_5$ core/shell NPs were collected by centrifugation and washed several times with acetone, then resolved in toluene. Au-$Ni_{12}P_5$ oligomer-like NPs were synthesized using the traditional seeded growth method for comparison. The details of the preparation procedure can be found in S1 (in the Electronic Supplementary Material (ESM)).

The crystal structures, morphologies, and chemical compositions of the prepared Au/$Ni_{12}P_5$ NPs were studied using X-ray diffraction (XRD, X'Pert Pro MPD system, Cu-Kα) and transmission electron microscopy (TEM, JEOL 2100FS with 200 kV field emission gun). The energy dispersive X-ray spectroscope (EDS) results are conducted with a field emission scanning electron

microscope (Zeiss Supra 55) to identify the elemental composition of the sample. X-ray photoelectron spectroscopy (XPS) measurements were performed using a VG ESCA LAB 220i-XL XPS system with a monochromatic Al Kα source. All XPS spectra were aligned using the C 1s core level peak (284.6 eV).

The electrocatalytic activities of the synthesized samples in alkaline solutions were characterized with electrochemical methods by a PARSTAT 4000 Potentiostats-Electrochemistry Workstation. The OER measurements were carried out in a three-electrode electrochemical cell containing 1 M KOH aqueous solution as the electrolyte with Pt foil as the counter electrode, and a saturated calomel electrode (SCE) as the reference electrode. To prepare the working electrode, the electroactive samples were mixed with CABOT VXC72 carbon black and Nafion. A loading mount of 25 μg of sample was prepared on a glassy carbon electrode (GCE) of 5 mm in diameter (~0.13 mg/cm^2). The polarization data tests were conducted at a scan rate of 5 mV/s between 0 and 0.8 V vs. SCE (about 1.1–1.9 V vs. reversible hydrogen electrode (RHE)). Electrochemical impedance spectroscopy (EIS) experiments were carried out from 100 kHz to 0.1 Hz at 1.57 V (vs. RHE).

3 Results and discussion

3.1 Morphology and structure

The prepared NPs were first identified as core/shell nanostructures by TEM characterization. From the TEM image in Fig. 1(a), the prepared samples are nearly spherical core/shell particles, with a core diameter of ~5 nm and a shell thickness of ~5.5 nm. High-resolution transmission electron microscopy (HR-TEM) was used to investigate the crystal structure of a single particle in detail (Fig. 1(b)). The lattice spacing measured in the shell is 0.186 and 0.217 nm, corresponding to the tetragonal $Ni_{12}P_5$ (312) and (040) planes. The crystal lattices in the shells are consecutive, indicating the single crystalline nature of the semiconductor shells, which is beneficial for ionic diffusion and electron transport [26].

The EDS results for the NPs are shown in Fig. 1(c). The atom ratio Ni:P:Au is calculated to be 68:30:2. The Ni/P atom ratio is 2.27, confirming the nickel phosphide phase is more likely to be $Ni_{12}P_5$ instead of Ni_2P. The ratio is less than the stoichiometric ratio for $Ni_{12}P_5$ (= 2.4). This is most likely due to some TPP residue coated on the NP surfaces. The weight ratio of

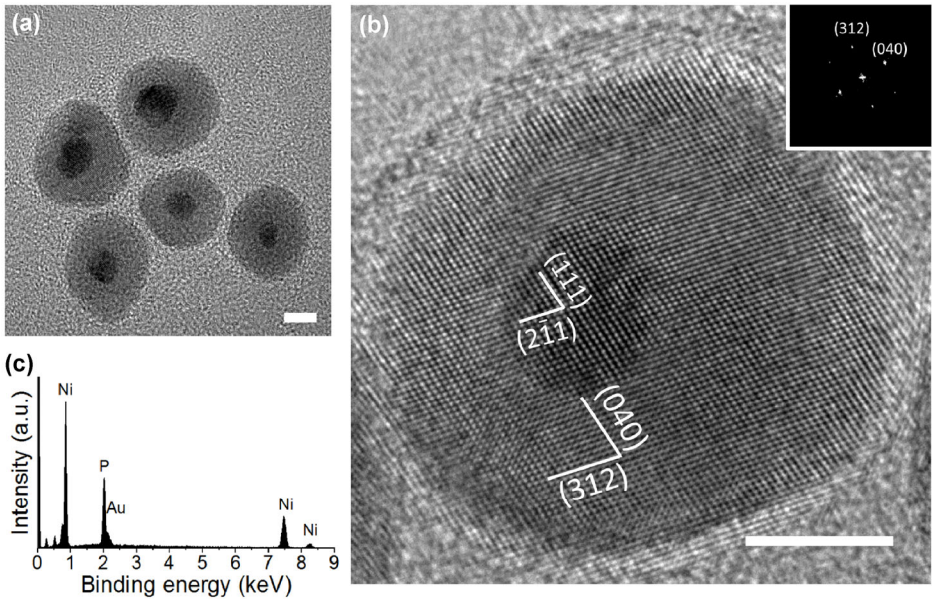

Figure 1 Structural characterizations of Au/$Ni_{12}P_5$ core/shell NPs. (a) The morphology of Au/$Ni_{12}P_5$ core/shell NPs revealed by TEM characterization. (b) HR-TEM image of an individual Au/$Ni_{12}P_5$ core/shell NP and the corresponding fast Fourier transformation (FFT) pattern (inset), confirming the single crystalline nature of the $Ni_{12}P_5$ shell. Scale bar: 5 nm. (c) The EDS spectrum of the synthesized Au/$Ni_{12}P_5$ NPs. The atom ratio of Ni:P:Au is confirmed to be 68:30:2.

Au:$Ni_{12}P_5$ is calculated to be 7.3:92.7, which is consistent with the results of the XRD Rietveld analysis.

Further evidence for the Au/$Ni_{12}P_5$ heterostructure was obtained by XRD. As shown in Fig. 2(a), all diffraction peaks can be indexed as the body-centered tetragonal (bct) phase of $Ni_{12}P_5$ (JCPDS No. 74-1381) and the face-centered cubic (fcc) phase of Au (JCPDS No. 89-3697), respectively. The grain sizes are estimated to be ~6 nm for the Au using the (002) peak and ~15 nm for the $Ni_{12}P_5$ using the (121) peak by Scherrer's equation, indicating the integrity of the crystal structure in the particles.

The phase composition and lattice parameters of the samples were evaluated by Rietveld analysis on the data of the XRD measurement. Estimation with Rietveld refinement implies that $Ni_{12}P_5$ makes up 92 wt.% (~97 vol.%) of the whole Au/$Ni_{12}P_5$ particle, with refined lattice parameters of tetragonal a = 0.8622 nm and c = 0.5129 nm. The calculated plane distance and the volume percentage of the $Ni_{12}P_5$ shell have a good agreement with the values directly observed from the TEM image. Referring to the lattice parameter data in the literature (JCPDS 89-3697, a = 0.8646 nm and c = 0.5070 nm), it could be inferred that the tetragonal crystal structure is a little extracted (~1.1%) in the c direction and contracted (~0.3%) in the a and b directions.

The chemical states of Ni and P in Au/$Ni_{12}P_5$ core/shell NPs were investigated by XPS, as shown in Figs. 2(b)–2(d). In nickel phosphides, electrons transfer from Ni to P. In Fig. 2(b), the Ni $2p_{1/2}$ binding energy around 853.3 eV is higher than the reported values for Ni metal (852.5–852.9 eV) and lower than those reported for Ni in NiO (853.5–854.1 eV) [28], indicating that the Ni cations in $Ni_{12}P_5$ possess a partial positive charge between 0 and 2 [29]. In the P 2p peak in Fig. 2(c), the P binding energy shifts to 129.5 eV for $2p_{3/2}$ and 130.5 eV for $2p_{1/2}$, slightly lower than the values for the neutral atom (about 130.4 eV for black phosphorus and 130.6 eV for red phosphorus [30]). The weak shoulder in the range of 131–133 eV indicates a slight amount of high oxidation state P, which may come from residual TPP. Figure 2(d) shows the binding energy peaks at 84.1 and 87.8 eV specific to Au $4f_{7/2}$ and Au $4f_{5/2}$, respectively. The characteristic features of these peaks show the presence of metallic gold in

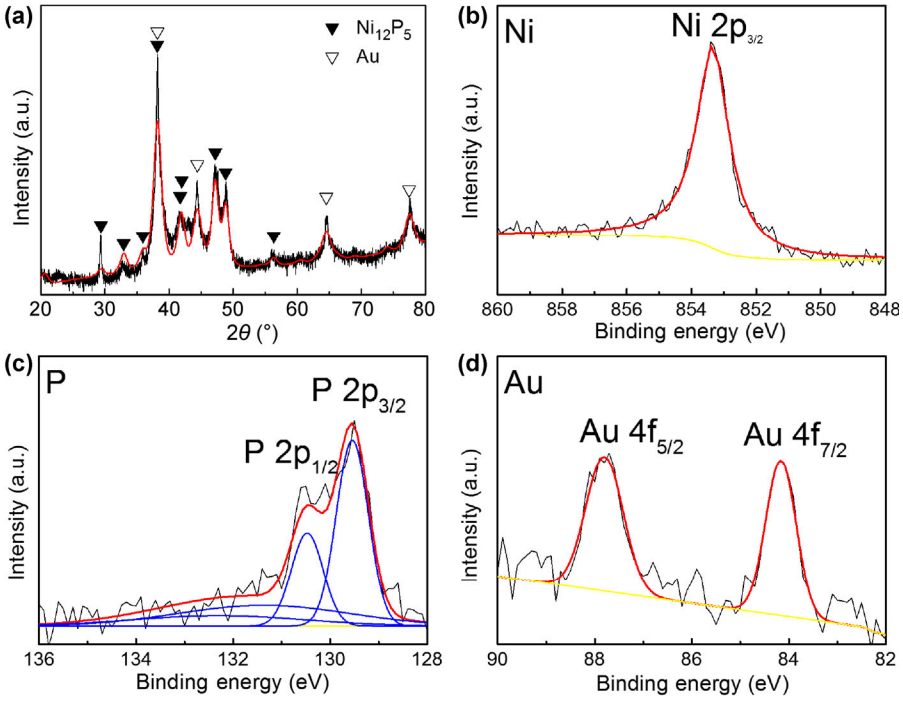

Figure 2 (a) The XRD pattern of the synthesized Au/$Ni_{12}P_5$ NPs. ▼: $Ni_{12}P_5$; ▽: Au. The simulation curve (red line) is calculated using Rietveld analysis based on the observed data (black line) of the measurement. (b)–(d) XPS spectra of Au/$Ni_{12}P_5$ core/shell NPs: (b) Ni 2p, (c) P 2p, and (d) Au 4f regions. Black line: observed data; red and blue lines: curve fitting; yellow line: background.

the NPs.

The Au-$Ni_{12}P_5$ oligomer-like and pure $Ni_{12}P_5$ NPs were also characterized using TEM. The morphology of the pure $Ni_{12}P_5$ NPs, Au-$Ni_{12}P_5$ oligomer-like and Au/$Ni_{12}P_5$ core/shell NPs are shown in Fig. 3. All three varieties of NP were of similar sizes (diameters of around 16 nm). Obviously, the differences in catalytic properties mainly come from the composition and structural differences due to the inclusion of Au.

3.2 Electrochemical properties of Au-modified $Ni_{12}P_5$ NPs

The OER activities of the nickel phosphide NPs with different nanostructures were investigated by electrochemical methods in alkaline solutions. All three nickel phosphide NPs behave as effective electrocatalysts towards OER, as illustrated in Fig. 4, and summarized in Table 1. From the polarization curves in Fig. 4(a),

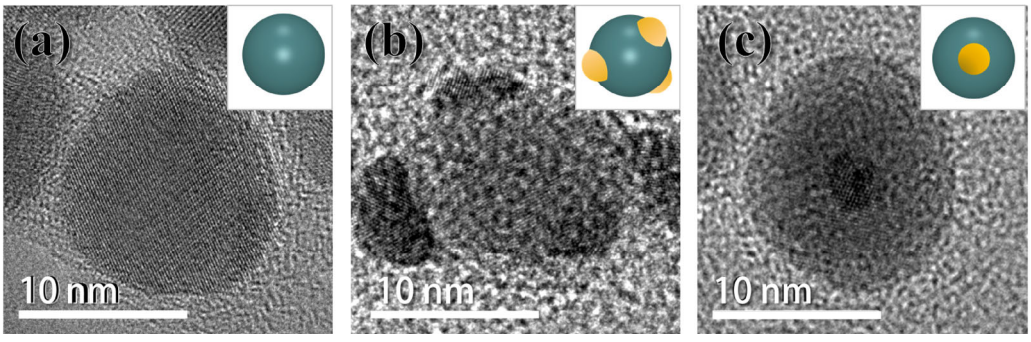

Figure 3 TEM characterization and structure schematic illustration of (a) pure $Ni_{12}P_5$ NPs; (b) Au-$Ni_{12}P_5$ oligomer-like NPs; and (c) Au/$Ni_{12}P_5$ core/shell NPs. Scale bar: 10 nm.

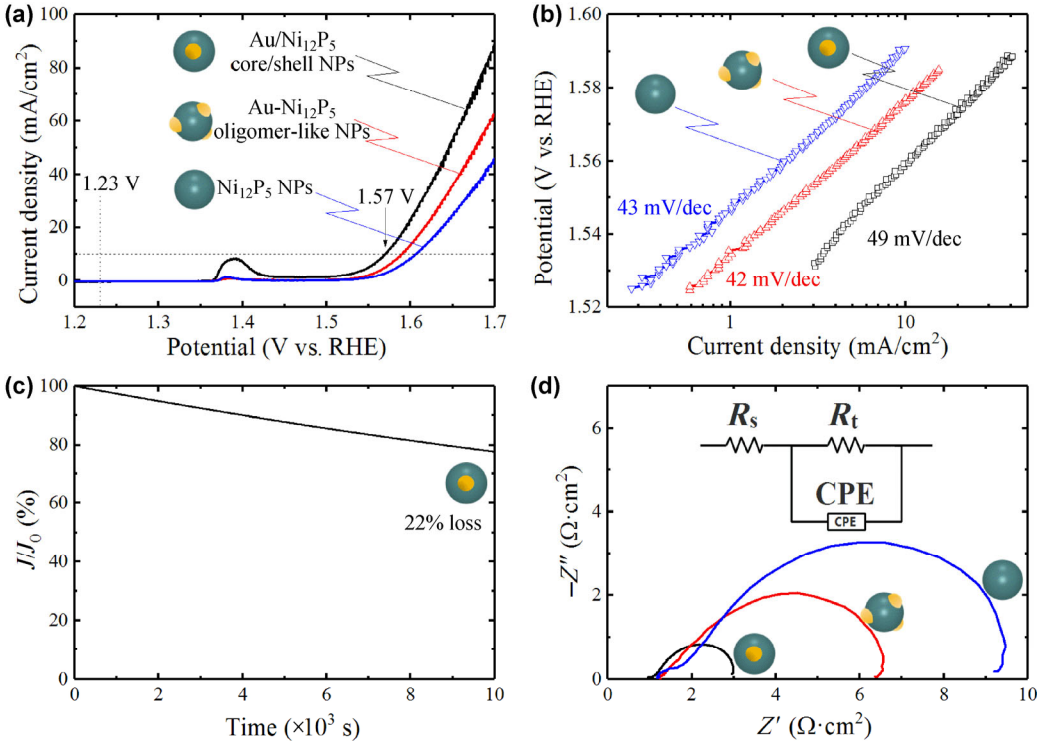

Figure 4 (a) Polarization curves, (b) Tafel plots and (d) Nyquist plots of reported Au/$Ni_{12}P_5$ core/shell NPs, Au-$Ni_{12}P_5$ oligomer-like NPs and pure $Ni_{12}P_5$ NPs loaded on a GCE in 1.0 M KOH solution. The loading amount of the catalysts on the GCE are 0.13 mg/cm^2. The Tafel plots have been corrected for the iR drop of the solution. Tafel slope are calculated to be 42–49 mV/dec by linear fitting. Inset of (d): the corresponding equivalent circuit diagram, consisting of R_s, R_t, and CPE. (c) Chronoamperometric response at a constant potential of 1.57 V for Au/$Ni_{12}P_5$ core/shell NPs.

Table 1 The OER catalytic parameters of the Au/$Ni_{12}P_5$ core/shell NPs, Au-$Ni_{12}P_5$ oligomer-like NPs and pure $Ni_{12}P_5$ NPs

	$Ni_{12}P_5$ NPs	Au-$Ni_{12}P_5$ oligomer-like NPs	Au/$Ni_{12}P_5$ core/shell NPs
Overpotential at j = 10 mA/cm^2 (V)	0.38	0.36	0.34
Tafel slope (mV/dec)	43	42	49
Electrolyte resistance R_s (Ω)	7.4	6.7	5.3
Charge-transfer resistance R_t (Ω)	46.6	28.8	11.4
CPE[a]: Y_0 (S·s^n)	0.0026	0.0021	0.016
CPE[a]: n	0.70	0.72	0.73

[a]The impedance of a CPE $Z_Q = (j\omega)^{-n}\cdot Y_0^{-1}$, where ω is the angular frequency in the circuit.

the inclusion of the Au core in the nickel phosphide shell has lowered the overpotential to 0.34 V at a current density of 10 mA/cm^2, which is comparable to the value for oxide catalysts such as Co_3O_4 (~0.31 V) [31]. This is obviously an improvement over Au-$Ni_{12}P_5$ oligomer-like (0.36 V) and pure $Ni_{12}P_5$ NPs (0.38 V). At room temperature with the same loading, the Au/$Ni_{12}P_5$ core/shell NPs exhibited an area-specific activity of 10 mA/cm^2 at 1.57 V (vs. RHE), which is 242% and 95% greater than that of pure $Ni_{12}P_5$ NPs (2.92 mA/cm^2) and Au-$Ni_{12}P_5$ oligomer-like NPs (5.14 mA/cm^2), respectively. It is obvious that the performance of $Ni_{12}P_5$ NP catalysts is greatly enhanced with the inclusion of Au, especially in the core/shell structure.

As shown in Fig. 4(b), all our NPs displayed a small Tafel slope, which is about 49, 42, and 43 mV/dec for Au/$Ni_{12}P_5$ core/shell, Au-$Ni_{12}P_5$ oligomer-like and pure $Ni_{12}P_5$ NPs, respectively. The relatively small Tafel slopes indicate the superior reaction kinetics and good catalytic activities of these nickel phosphide NPs. For example, some well-known OER catalysts have Tafel slopes of 40 mV/dec (pure RuO_2), 60 mV/dec (pure IrO_2) [7] and 70 mV/dec (Co_3O_4 hybrid system) [4]. The Tafel slopes of our samples are comparable or even lower than some known OER catalysts.

The oxidation peak at the voltage of ~1.39 V can be associated with the Ni^{2+}/Ni^{3+} couple, which is common in some Ni contained systems [32]. To confirm this, we measured the cyclic voltammogram (CV) curve, in which a pair of Ni^{2+}/Ni^{3+} redox peaks can be observed (see S2 and Fig. S1 in the ESM), indicating good reversibility after the oxidation reaction. An oxidation peak is located at ~1.38 V, indicating the oxidation of Ni^{2+} to Ni^{3+} in $Ni_{12}P_5$, and the initial absorption of –O or –OH to Ni atoms at the catalyst surface before the oxygen evolution, which is common in the OER process (as depicted in previous studies [33, 34]).

The chronoamperometric response at a constant potential of 1.57 V for the Au/$Ni_{12}P_5$ core/shell NPs was recorded, as shown in Fig. 4(d). The OER activity is reserved with an anodic current attenuation of 22% after 10^4 s. The NPs demonstrate considerable durability in alkaline electrolytes, however there is still room for better performance with improved adhesion of the powder to the electrode.

These results demonstrate that the different $Ni_{12}P_5$ based NPs, i.e. Au/$Ni_{12}P_5$ core/shell, Au-$Ni_{12}P_5$ oligomer-like and pure $Ni_{12}P_5$ NPs, are all efficient catalysts for OER, of which the Au/$Ni_{12}P_5$ core/shell NPs are the most effective. To identify the exact electrical conductivity of the three electrodes and investigate the structure-property relationships, electrochemical impedance spectra were first measured at room temperature over a frequency range from 100 kHz to 0.1 Hz under open-circuit conditions. As the semi-circular Nyquist plots show in Fig. 4(d), the system was typically modeled with an equivalent circuit model consisting of an electrolyte resistance (R_s), a charge-transfer resistance (R_t) and a constant-phase element (CPE) (shown in Fig. 4(d) inset) and simulated by Zview software. The Faradaic resistance (charge-transfer resistance) R_t of the samples, which intuitively corresponds to the circular diameter in Nyquist plots, represents the resistance from the mass transfer during electrocatalytic reactions, which is an important reference for the reaction efficiency of the electrode [21, 35]. R_t was calculated to be 46.6 Ω for pure $Ni_{12}P_5$ NPs, 28.8 Ω for Au-$Ni_{12}P_5$ oligomer-like NPs and 11.4 Ω for the Au/$Ni_{12}P_5$ core/shell NPs. Obviously, core/shell NPs have the lowest charge-transfer resistance among the three samples, which can be attributed to the enhanced electric conductivity and short charge diffusion length due to the synergistic effect. This is in good agreement with the fact that the core/shell

crystals display the highest catalytic activity.

The capacitance-like Y_0 of CPE reflects the double layer capacitance (C_d) at the surface of the NPs. The double layer capacitances often reflect the position of absorbed molecules, which is related to the effective area of the surface. The value of Y_0 for the core/shell crystal is much larger than the Au-$Ni_{12}P_5$ oligomer-like and pure $Ni_{12}P_5$ NPs, as shown in Table 1. By simplifying the model to R(CR) using C_d instead of Y_0, we can compare the double layer capacitances C_d of the three structures by simulation. In fact, C_d can be deduced by

$$C_d = 1/\omega_B R_t \quad (1)$$

directly, where ω_B is the angular frequency at the top point of each semicircle. The double layer capacitance of 0.97 mF for pure $Ni_{12}P_5$ NPs and 1.1 mF for oligomer-like NPs are very close, while the Au/$Ni_{12}P_5$ core/shell NPs show a much larger capacitance of 11.0 mF. The Au cores could multiply the double layer capacitance of the $Ni_{12}P_5$ NPs by 10. This result discloses the distinct microstructural differences between the core/shell and oligomer-like NPs. For our NPs with similar size and phase, the much larger double layer capacitance of the Au/$Ni_{12}P_5$ core/shell NPs implies a higher concentration of electroactive positions at the surface, which reflect the difference of the electrical structure in the shell.

3.3 Synergetic effect in the single crystalline core/shell structure

Heterostructures have attracted great interest in catalytic enhancement due to the potential synergetic effect. The single crystal nature of the $Ni_{12}P_5$ shells and lattice modulation between Au and $Ni_{12}P_5$ play an important role in their electrocatalytic performance. It is known that the single crystalline semiconductor shell benefits the study of semiconductor physics at the nanoscale and promotes research on technological devices with optimum physicochemical properties [25, 26]. Crystalline defects in the semiconductor shell weaken nanomaterial properties and degrade device performance. As shown in Fig. 1(b) and many similar HR-TEM images, the $Ni_{12}P_5$ forms a single crystal, which favors ionic diffusion and electron transport, and is accordingly beneficial for its OER activity. On the other hand, lattice-engineered interfacial effects between Au and $Ni_{12}P_5$ also affect the electronic and catalytic properties of nanoparticles. As Fig. 1(b) shows, the lattice spacing of the Au (111) facets was measured to be 0.217 nm, which is 7.9% less than its standard value (0.235 nm), indicating that the Au (111) facets are suppressed by the outer $Ni_{12}P_5$ shells. The atomic positions drift away from the normal lattice points, creating strain or other structural changes. Such changes affect the electronic and catalytic properties of the nanoparticles. Moreover, the dislocations and lattice strains can be clearly observed. With this tensile stress exerted by the Au core support, the shell overlayer undergoes structural distortion which may result in tuning the d-band center and the adsorbate binding energy in the surface [36].

In addition, the lattice matching between Au and $Ni_{12}P_5$ could also be verified by the lattice continuity between Au and $Ni_{12}P_5$. The orientation relationships between the fcc Au core and the bct $Ni_{12}P_5$ shell were determined as $Ni_{12}P_5$(312)//Au(210) and $Ni_{12}P_5$(040)//Au(111), as illustrated in Fig. 1(b). The lattice matching between metal core and semiconductor shell serve as efficient electron channels during the reaction, correspondingly enhancing its catalytic performance.

Finally, the electrical coupling effect from Au will increase the proportion of high oxidation state metal atoms in the surface, which are essential intermediates in OER. For our NP catalyst, when the metallic Au and nickel phosphide shell are in contact, the free electrons will transfer between them due to the work function difference. As a highly electronegative transition metal, Au can act as an electron sink to facilitate the oxidation [23]. Compared to the oligomer-like structure, the Au core in the core/shell structure can affect the whole surface of the NPs, which may be more helpful for OER.

3.4 Catalytic mechanism of metal phosphides as OER electrocatalysts

$Ni_{12}P_5$ has a body-centered tetragonal structure with lattice constant of a = 0.86 nm and c = 0.51 nm, as shown in Fig. 5(a). The Ni–P bond lengths vary between 0.22–0.26 nm. The P atoms have two equivalent sites in $Ni_{12}P_5$: One is located at the vertex and body-center positions (2a Wyckoff position) with an 8-Ni-atom

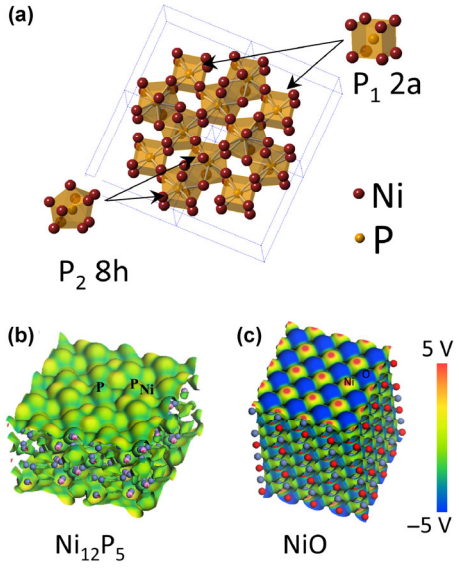

Figure 5 (a) The structure schematic of the $Ni_{12}P_5$ lattice. Calculated total electron density of the (b) $Ni_{12}P_5$ (001) surface and (c) NiO (001) surface, mapped by the electrostatic potential. The isosurface value is 0.2 e/Å^3. Electrostatic potential is color coded as in the scale bar: The blue corresponds to negatively charged regions, while the red represents positively charged regions. (Color of atoms: navy, Ni; pink, P; red, O.)

cuboid; the other is located at the 8h Wyckoff position with a 10-Ni-atom tetrakaidekahedron. For binary nickel phosphides, it has been reported that the electronic polarizability of phosphorus atoms will increase with coordination to the neighboring Ni atoms [28]. The high average P–Ni coordination number (8 and 10) in $Ni_{12}P_5$ results in the metallic behavior, which might also explain the improved OER efficiency.

The covalent bonding nature in $Ni_{12}P_5$ was calculated using first-principles calculations using Vienna *Ab initio* Simulation Package (VASP) [37, 38]. As supported by the Bader charge analysis [39, 40], there are about 0.16 electrons transferred from each surface Ni atom to neighboring P atoms, suggesting a dominant covalent bond character. It is also notable that the variation of electrostatic potential in $Ni_{12}P_5$ surface is within 1 V, as shown in Fig. 5(b). In principle, regions with positive electrostatic potential may become hydride acceptors, which are usually the sites of Ni atoms. This weak electrostatic potential distribution and the covalent bonding nature of Ni-P might explain the relatively weaker adsorption sites at the $Ni_{12}P_5$ surface, and therefore the improved OER activity. It is also noted that the NiO compound has been proposed as a promising electrocatalyst. In contrast, the bonding character in the NiO surface is predominantly ionic, with a much larger variation of electrostatic potential, as shown in Fig. 5(c). This leads to strong binding of OH* groups at the surface. For NiO, it has been calculated that the binding energy is too strong (at low coverage) to reach the theoretical best catalyst activities [33, 41]. Thus, we can expect improved OER activity with $Ni_{12}P_5$ compared with that with NiO.

4 Conclusion

Based on detailed structural and electrochemical study, we find improved OER catalytic activity using Au/$Ni_{12}P_5$ NPs compared to previously reported electrocatalysts, which is ascribed to their weak hydride accepting ability at the surface, and strong interfacial coupling between the crystalline metallic cores and the thin semiconductor shells. Our results suggest that these NPs could find use as promising electrocatalysts for water splitting applications.

Acknowledgements

This work was supported by the National Natural Science Foundation of China (Nos. 11674023, 51371015, 51331002, and 51501004), the Beijing Municipality Natural Science Foundation (No. 2142018), and the Fundamental Research Funds for the Central Universities (No. FRF-BR-15-023A). We would like to thank Prof. Feng Yuanping at Centre for Advanced 2D Materials and Graphene Research of NUS for discussions on computing results. We also thank the National Supercomputing Centre Singapore for providing the computing resource.

Electronic Supplementary Material: Supplementary material (the details of the sample preparation and the calculation methods, the CV characteristic curve and extra TEM images) is available in the online version of this article at http://dx.doi.org/10.1007/s12274-017-1527-1.

References

[1] Gray, H. B. Powering the planet with solar fuel. *Nat. Chem.* **2009**, *1*, 7.

[2] Kanan, M. W.; Nocera, D. G. *In situ* formation of an oxygen-evolving catalyst in neutral water containing phosphate and Co^{2+}. *Science* **2008**, *321*, 1072–1075.

[3] Singh, R. N.; Mishra, D.; Anindita; Sinha, A. S. K.; Singh, A. Novel electrocatalysts for generating oxygen from alkaline water electrolysis. *Electrochem. Commun.* **2007**, *9*, 1369–1373.

[4] Ma, T. Y.; Dai, S.; Jaroniec, M.; Qiao, S. Z. Metal-organic framework derived hybrid Co_3O_4-carbon porous nanowire arrays as reversible oxygen evolution electrodes. *J. Am. Chem. Soc.* **2014**, *136*, 13925–13931.

[5] Cui, B.; Lin, H.; Li, J. B.; Li, X.; Yang, J.; Tao, J. Core-ring structured $NiCo_2O_4$ nanoplatelets: Synthesis, characterization, and electrocatalytic applications. *Adv. Funct. Mater.* **2008**, *18*, 1440–1447.

[6] Suntivich, J.; May, K. J.; Gasteiger, H. A.; Goodenough, J. B.; Shao-Horn, Y. A perovskite oxide optimized for oxygen evolution catalysis from molecular orbital principles. *Science* **2011**, *334*, 1383–1385.

[7] Mattos-Costa, F. I.; de Lima-Neto, P.; Machado, S. A. S.; Avaca, L. A. Characterisation of surfaces modified by sol-gel derived $Ru_xIr_{1-x}O_2$ coatings for oxygen evolution in acid medium. *Electrochim. Acta* **1998**, *44*, 1515–1523.

[8] Over, H. Surface chemistry of ruthenium dioxide in heterogeneous catalysis and electrocatalysis: From fundamental to applied research. *Chem. Rev.* **2012**, *112*, 3356–3426.

[9] Zhou, W. J.; Wu, X. J.; Cao, X. H.; Huang, X.; Tan, C. L.; Tian, J.; Liu, H.; Wang, J. Y.; Zhang, H. Ni_3S_2 nanorods/Ni foam composite electrode with low overpotential for electrocatalytic oxygen evolution. *Energy Environ. Sci.* **2013**, *6*, 2921–2924.

[10] Zhang, Y. Q.; Ouyang, B.; Xu, J.; Jia, G. C.; Chen, S.; Rawat, R. S.; Fan, H. J. Rapid synthesis of cobalt nitride nanowires: Highly efficient and low-cost catalysts for oxygen evolution. *Angew. Chem., Int. Ed.* **2016**, *55*, 8670–8674.

[11] Cao, X. Y.; Wang, H. N.; Lu, S. F.; Chen, S.; Xiang, Y. An Ni–P/C electro-catalyst with improved activity for the carbohydrazide oxidation reaction. *RSC Adv.* **2016**, *6*, 91956–91959.

[12] Wang, H. N.; Cao, D.; Xiang, Y.; Liang, D. W.; Lu, S. F. Novel Pd-decorated amorphous Ni–B/C catalysts with enhanced oxygen reduction reaction activities in alkaline media. *RSC Adv.* **2014**, *4*, 51126–51132.

[13] Surendranath, Y.; Kanan, M. W.; Nocera, D. G. Mechanistic studies of the oxygen evolution reaction by a cobalt-phosphate catalyst at neutral pH. *J. Am. Chem. Soc.* **2010**, *132*, 16501–16509.

[14] Song, H.; Dai, M.; Song, H. L.; Wan, X.; Xu, X. W.; Jin, Z. S. A solution-phase synthesis of supported Ni_2P catalysts with high activity for hydrodesulfurization of dibenzothiophene. *J. Mol. Catal. A-Chem.* **2014**, *385*, 149–159.

[15] Oyama, S. T. Novel catalysts for advanced hydroprocessing: Transition metal phosphides. *J. Catal.* **2003**, *216*, 343–352.

[16] Mi, K.; Ni, Y. H.; Hong, J. M. Solvent-controlled syntheses of $Ni_{12}P_5$ and Ni_2P nanocrystals and photocatalytic property comparison. *J. Phys. Chem. Solids* **2011**, *72*, 1452–1456.

[17] Ni, Y. H.; Liao, K. M.; Li, J. *In situ* template route for synthesis of porous $Ni_{12}P_5$ superstructures and their applications in environmental treatments. *CrystEngComm* **2010**, *12*, 1568–1575.

[18] Liu, P.; Rodriguez, J. A. Catalysts for hydrogen evolution from the [NiFe] hydrogenase to the $Ni_2P(001)$ surface: The importance of ensemble effect. *J. Am. Chem. Soc.* **2005**, *127*, 14871–14878.

[19] Popczun, E. J.; McKone, J. R.; Read, C. G.; Biacchi, A. J.; Wiltrout, A. M.; Lewis, N. S.; Schaak, R. E. Nanostructured nickel phosphide as an electrocatalyst for the hydrogen evolution reaction. *J. Am. Chem. Soc.* **2013**, *135*, 9267–9270.

[20] Paseka, I. Hydrogen evolution reaction on Ni-P alloys: The internal stress and the activities of electrodes. *Electrochim. Acta* **2008**, *53*, 4537–4543.

[21] Huang, Z. P.; Chen, Z. B.; Chen, Z. Z.; Lv, C. C.; Meng, H.; Zhang, C. $Ni_{12}P_5$ nanoparticles as an efficient catalyst for hydrogen generation via electrolysis and photoelectrolysis. *ACS Nano* **2014**, *8*, 8121–8129.

[22] Zhang, G.; Wang, G. C.; Liu, Y.; Liu, H. J.; Qu, J. H.; Li, J. H. Highly active and stable catalysts of phytic acid-derivative transition metal phosphides for full water splitting. *J. Am. Chem. Soc.* **2016**, *138*, 14686–14693.

[23] Yeo, B. S.; Bell, A. T. Enhanced activity of gold-supported cobalt oxide for the electrochemical evolution of oxygen. *J. Am. Chem. Soc.* **2011**, *133*, 5587–5593.

[24] Wu, J. B.; Li, P. P.; Pan, Y. T.; Warren, S.; Yin, X.; Yang, H. Surface lattice-engineered bimetallic nanoparticles and their catalytic properties. *Chem. Soc. Rev.* **2012**, *41*, 8066–8074.

[25] Zhang, J. T.; Tang, Y.; Lee, K.; Ouyang, M. Nonepitaxial growth of hybrid core–shell nanostructures with large lattice mismatches. *Science* **2010**, *327*, 1634–1638.

[26] Duan, S. B.; Wang, R. M. Au/$Ni_{12}P_5$ core/shell nanocrystals from bimetallic heterostructures: *In situ* synthesis, evolution and supercapacitor properties. *NPG Asia Mater.* **2014**, *6*, e122.

[27] Carenco, S.; Portehault, D.; Boissière, C.; Mézailles, N.; Sanchez, C. 25th anniversary article: Exploring nanoscaled matter from speciation to phase diagrams: Metal phosphide nanoparticles as a case of study. *Adv. Mater.* **2014**, *26*, 371–389.

[28] Franke, R. X-ray absorption and photoelectron spectroscopy investigation of binary nickel phosphides. *Spectrochim. Acta A-Mol. Biomol. Spectrosc.* **1997**, *53*, 933–941.

[29] Wu, S. K.; Lai, P. C.; Lin, Y. C. Atmospheric hydrodeoxygenation of guaiacol over nickel phosphide catalysts: Effect of phosphorus composition. *Catal. Lett.* **2014**, *144*, 878–889.

[30] Franke, R.; Chassé, T.; Streubel, P.; Meisel, A. Auger parameters and relaxation energies of phosphorus in solid compounds. *J. Electron Spectrosc. Relat. Phenom.* **1991**, *56*, 381–388.

[31] Liang, Y. Y.; Li, Y. G.; Wang, H. L.; Zhou, J. G.; Wang, J.; Regier, T.; Dai, H. J. Co_3O_4 nanocrystals on graphene as a synergistic catalyst for oxygen reduction reaction. *Nat. Mater.* **2011**, *10*, 780–786.

[32] Su, X. R.; Xu, Y. Y.; Liu, J. L.; Wang, R. M. Controlled synthesis of $Ni_{0.25}Co_{0.75}(OH)_2$ nanoplates and their electrochemical properties. *CrystEngComm* **2015**, *17*, 4859–4864.

[33] Rossmeisl, J.; Qu, Z. W.; Zhu, H.; Kroes, G. J.; Nørskov, J. K. Electrolysis of water on oxide surfaces. *J. Electroanal. Chem.* **2007**, *607*, 83–89.

[34] Rossmeisl, J.; Logadottir, A.; Nørskov, J. K. Electrolysis of water on (oxidized) metal surfaces. *Chem. Phys.* **2005**, *319*, 178–184.

[35] Hu, J. M.; Zhang, J. Q.; Cao, C. N. Oxygen evolution reaction on IrO_2-based DSA® type electrodes: Kinetics analysis of Tafel lines and EIS. *Int. J. Hydrogen Energy* **2004**, *29*, 791–797.

[36] Hammer, B.; Nørskov, J. K. Theoretical surface science and catalysis—Calculations and concepts. *Adv. Catal.* **2000**, *45*, 71–129.

[37] Kresse, G.; Furthmüller, J. Efficiency of *ab-initio* total energy calculations for metals and semiconductors using a plane-wave basis set. *Comput. Mater. Sci.* **1996**, *6*, 15–50.

[38] Kresse, G.; Furthmüller, J. Efficient iterative schemes for *ab initio* total-energy calculations using a plane-wave basis set. *Phys. Rev. B* **1996**, *54*, 11169–11186.

[39] Yu, M.; Trinkle, D. R. Accurate and efficient algorithm for Bader charge integration. *J. Chem. Phys.* **2011**, *134*, 064111.

[40] Tang, W.; Sanville, E.; Henkelman, G. A grid-based Bader analysis algorithm without lattice bias. *J. Phys.: Condens. Matter* **2009**, *21*, 084204.

[41] Man, I. C.; Su, H. Y.; Calle-Vallejo, F.; Hansen, H. A.; Martínez, J. I.; Inoglu, N. G.; Kitchin, J.; Jaramillo, T. F.; Nørskov, J. K.; Rossmeisl, J. Universality in oxygen evolution electrocatalysis on oxide surfaces. *ChemCatChem* **2011**, *3*, 1159–1165.